NUCLEATE POOL BOILING OF R-134A ON ENHANCED HORIZONTAL SURFACES HAVING PORES ON SUB-TUNNELS

Anadi Mondal & Nae-Hyun Kim[*]

Department of Mechanical Engineering, Incheon National University, 12-1 Songdo-Dong, Yeonsu-Gu Inchon, 22012, Korea

*Address all correspondence to: Nae-Hyun Kim, Department of Mechanical Engineering, Incheon National University, 12-1 Songdo-Dong, Yeonsu-Gu Inchon, 22012, Korea, E-mail: knh0001@incheon.ac.kr

Enhanced surfaces having circular pores and rectangular sub-tunnels were made and nucleate boiling tests were conducted using R-134a under horizontal positions. Nine samples had pore diameters from 0.1 mm to 0.3 mm and pore pitches from 0.75 mm to 3.0 mm. The heat transfer coefficient increased as the pore size increased, at least for the investigated test range. The reason was attributed to the increased bubble departure diameter with the pore diameter. The heat transfer coefficient also increased as the pore pitch decreased, while the number of pores increased approximately in proportion to the square of pitch ratio. Increased nucleate site density at smaller pore pitch appears responsible for the high heat transfer coefficient. Existing theoretical models did not adequately predict the present data. A new model was proposed, which predicted 70% of the present data within $\pm$ 50%.

KEY WORDS: *pore, sub-tunnel, enhanced surface, nucleate pool boiling, R-134a*

1. INTRODUCTION

Special structured enhanced boiling tubes are widely used in refrigeration and process industries. These tubes are made from low fin tubes, whose fins are further deformed to provide a pore/sub-tunnel structure. Due to their wide usage, a significant amount of research has been conducted to investigate the boiling performances and the related heat transfer mechanisms. The investigations may be divided into those on the tubes and those on the plates.

As for the investigations on tubes, Webb and Pais (1992) obtained nucleate pool boiling data of R-11, R-12, R-22, R-123, and R-134a on several commercial enhanced tubes. The heat transfer coefficients of the high-pressure refrigerants (R-12, R-22, and R-134a) were higher than those of the low pressure refrigerants (R-11 and R-123). A systematic study on the boiling performance of tubes having surface pores/sub-tunnels was performed by Chien and Webb (1998a,b), who investigated the effect of pore diameter, pore pitch, and tunnel shape using R-11 and R-123. There was an optimum pore diameter and pore pitch for a specific heat flux range. At a low heat flux, tubes having small pore diameter and large pore pitch yielded higher heat transfer coefficients, while, at a high heat flux, the opposite was true. If the pore diameter is too large at a low heat flux, the tunnel is likely to be flooded by the liquid, and the heat transfer coefficient is decreased. If the pre-diameter is too small at a high heat flux, the tunnel will dry out due to

NOMENCLATURE

A	heat transfer area (m^2) or bubble dimension (m)			interface
			T	temperature (K)
B	bubble dimension (m)		t	time (s)
Bo	Bond number [$= d_p^2(\rho_l - \rho_v)g/\sigma$]		V	volume (m^3)
C	bubble dimension (m)		W	tunnel width (m)
c_p	specific heat (J/kgK)			
D	bubble dimension (m)		**Greek Symbols**	
d_b	bubble departure diameter (m)		δ_{ne}	non-evaporating liquid film thickness (m)
d_p	pore diameter (m)			
E	bubble dimension (m)		ΔT	wall superheat (K)
f	bubble generation frequency (1/s)		ρ	density (kg/m^3)
g	gravitational constant (m/s^2)		σ	surface tension (N/m)
H	tunnel height (m)			
h	heat transfer coefficient (W/m^{2}K)		**Subscripts**	
i_{lv}	heat of vaporization (J/kg)		0	initial time
k	thermal conductivity (W/mK)		ex	external
L	tunnel length (m)		exp	experimental
m	mass (kg)		f	fin
N	number of pores		g	growth period
N_A	mean density of active nucleation sites (1/m^2)		l	liquid
			m	mean
N_m	number of meniscus in the tunnel		p	pore
P	pressure (N/m^2) or pitch (m)		$pred$	prediction
Pr	Prandtl number		sat	saturation
q	heat flux (W/m^2)		tip	tip
R	gas constant (J/kgK)		tun	tunnel
R_m	meniscus radius (m)		v	vapor
s	coordinate along liquid–vapor		w	wall or waiting period

the insufficient liquid supply. The flow visualization studies on these tubes by Chien and Webb (1998c,d) supported the trend. The dry-out of the tunnel at a high heat flux and the flooding of the tunnel at a low heat flux were observed. Kim and Choi (2001) provided nucleate pool boiling test results for tubes having triangular pores and gourd-shaped tunnels. Test results using R-11, R-123, and R-134a showed that preferred pore size depended on the refrigerant. Additional data on nucleate boiling heat transfer coefficient on the enhanced geometry are available from Chen et al. (2005), Yang and Fan (2006), Ribatski and Thome (2006), Gorgy and Eckels (2012), Rooyen and Thome (2013), Orman (2016), and Balaji et al. (2018).

As for the investigations on plate geometry, Nakayama et al. (1980a) investigated the pool boiling performance of the horizontal enhanced surfaces using R-11, water, and nitrogen. The enhanced surfaces had triangular pores/sub-tunnels. Approximately 80% to 90% reduction of the wall superheat was possible compared with those of the plain surface. The optimum pore diameter was different depending on the refrigerant: 0.14 mm for water, 0.10 mm for water, and

0.09 mm for nitrogen. Pastuszko and Wojcik (2015) made enhanced boiling surfaces by sintering a perforated foil on three-dimensional micro-fins, and tested using water and FC-72 in a horizontal position. Both for water and FC-72, the highest heat transfer coefficients were obtained with pores of 0.3 mm diameter. Chien and Chang (2004) investigated the pool boiling performance of the enhanced surfaces in a vertical position. The surfaces had triangular pores/sub-tunnels, and were tested using water and HFC-4310. For water boiling, the preferred fin height was 0.7 mm and preferred pore pitch was 1.0 mm. For HFC-4310, the fin height and pore pitch had no significant influence.

Only limited studies are available about the modeling of nucleate boiling on enhanced surfaces. Nakayama et al. (1980b) were the first to develop a semi-empirical model. They assumed that the main mechanism of heat transfer inside sub-tunnels was an evaporation of thin liquid meniscus at the sharp corners. Using the experimental data, they developed a model, which included the bubble departure diameter, and bubble generation frequency. Chien and Webb (1998e) modified several features of the Nakayama et al. model. The improvements included the formulation of the liquid menisci evolution and modeling of the bubble departure diameter.

Successive improvements were made by Ramaswamy et al. (2003) by including the dynamic bubble departure diameter model. Pastuszko and Wojcik (2015) proposed a rather simple model, where the bubble growth period was assumed to be three times that of the waiting period, and the number of active pores was determined from the pore geometry. Note that all the existing models are based on horizontal surface with circular pores. Thus, to test the accuracy of the models, data from horizontal surfaces with circular pores are necessary. However, the above literature survey shows that most of the existing experimental data are for tube geometry. Although Nakayama et al. (1980a) tested plates under a horizontal position, their pore shapes were triangular (not circular). This suggests that more data are needed from the surface having circular pores. In this study, nine enhanced surfaces having circular pores/rectangular sub-tunnels were made, and tests were conducted under horizontal position using R-134a. Then, the obtained data were compared with predictions of existing models.

2. TEST SAMPLES

The test samples were made from copper blocks of 10 mm × 10 mm × 5 mm (Fig. 1). Nine samples had different pore pitch (0.75 mm, 1.5 mm, and 3.0 mm) and different pore diameter (0.1 mm, 0.2 mm, and 0.3 mm). The samples were identified as 0.1/0.75, 0.1/1.5, 0.1/3.0, 0.2/0.75, 0.2/1.5, 0.2/3.0, 0.3/0.75, 0.3/0.15, and 0.3/3.0, where the first number indicates pore diameter, and the second number indicates pore pitch. Cross-sectional photos of the samples are also shown in Fig. 1. Sub-tunnels having dimensions of 0.4 mm width and 1.0 mm height were fabricated by wire-cutting at 0.1 mm underneath the boiling surface.

A schematic drawing of the test section is shown in Fig. 2. At one side of the block, four holes of 1.0 mm diameter were drilled to the center of the block to insert thermocouples. The holes were located 2.0 mm below the tunnel bottom. When inserting the thermocouple (Co-Cu, 0.3 mm diameter), silver epoxy (Chromalox HTRC) was coated on the thermocouple to fill the voids in the hole. The copper block was heated using the plate heater (surface mount chip resistor, Component General CCR-375-1, 29 Ohm), which can sustain a heat flux up to 3800 kW/m^2. The plate heater was silver soldered to the copper block to minimize the interfacial thermal resistance. Then, the copper block was enclosed in the MCN (Monomer Cast Nylon) block of 30 mm × 30 mm × 20 mm (Fig. 2). The MCN has a low thermal conductivity of approximately 0.4 W/mK.
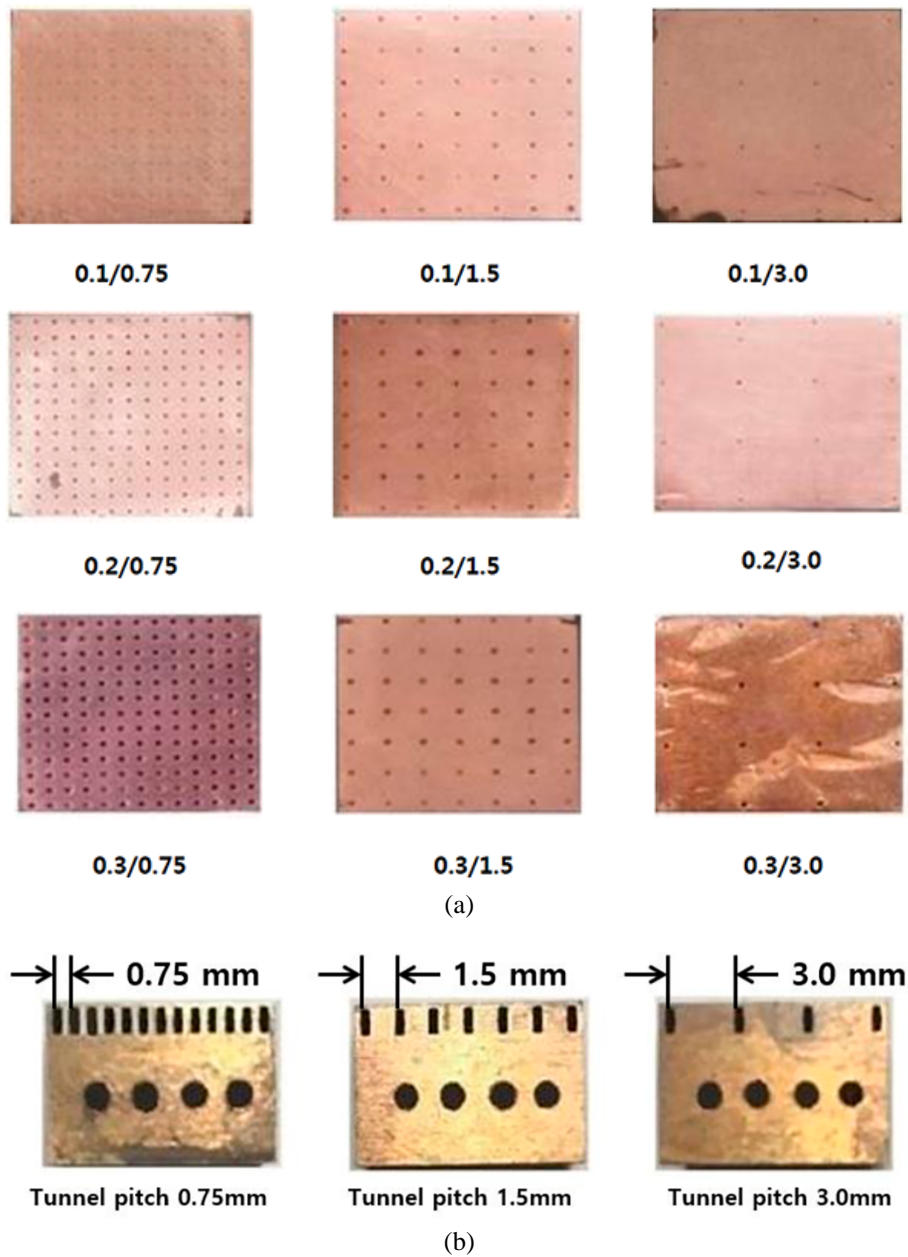
0.1/0.75   0.1/1.5   0.1/3.0

0.2/0.75   0.2/1.5   0.2/3.0

0.3/0.75   0.3/1.5   0.3/3.0

(a)

0.75 mm   1.5 mm   3.0 mm

Tunnel pitch 0.75mm   Tunnel pitch 1.5mm   Tunnel pitch 3.0mm

(b)

FIG. 1: Photos of the test samples. (a) Photos of the samples. Numbers are pore pitch (mm)/pore diameter (mm). (b) Cross-section of the test samples.

The gap between the copper block and the MCN was filled with an epoxy. The heat loss through the MCN block was estimated using one-dimensional heat conduction equation. The heat loss was less than 0.3% of the total heat input, and thus neglected in the heat flux calculation.

(a)

(b)
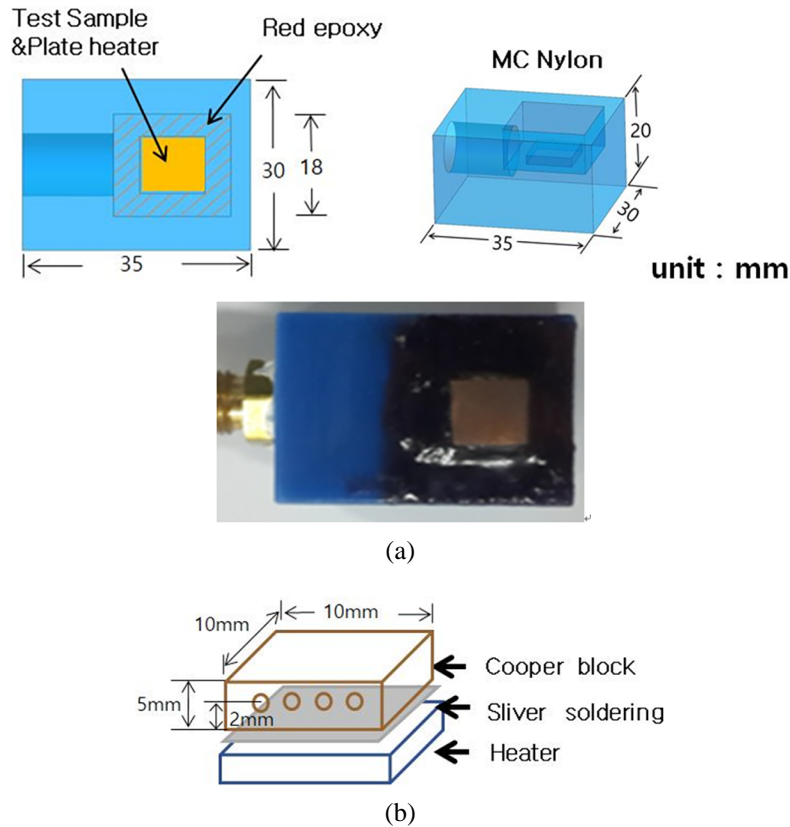
FIG. 2: (a) Schematic drawing and photo of the test section, (b) details of the test sample

3. EXPERIMENTAL APPARATUS AND PROCEDURES

The test apparatus is shown in Fig. 3. The pool boiling test cell had a rectangular shape of 160 mm $\times$ 176 mm $\times$ 196 mm, which was made by welding stainless steel plates of 20 mm thickness. At one side of the cell, a glass window of 110 mm diameter was mounted for visualization of bubbles generated from the test sample. Bubble behaviors were photographed using a high speed camera (IDT Vision, iN8-S2, 32,000 fps). Vapor temperatures were measured at two locations. Liquid temperatures were also measured at two locations: 20 mm above the test sample and 20 mm below the test sample. During the test, the four temperatures agreed within 0.2°C.

A pressure transducer (Setra C206, 0 $\sim$ 1000 psi) was installed on top of the test cell to measure the vapor pressure. When the measured pressure was converted to the corresponding saturation temperature, the saturation temperature agreed with the measured vapor temperature within 0.3°C. Two water coils, one in the vapor, another in the liquid, were inserted in the cell to control the vapor and the liquid temperature. A cartridge heater was mounted underneath the test sample, which was used to maintain the liquid pool temperature.

The test procedure is described in detail in Kim and Choi (2000), and a brief summary is provided here. Tests were performed at two saturation temperatures (4.4°C and 26.7°C). The 4.4°C
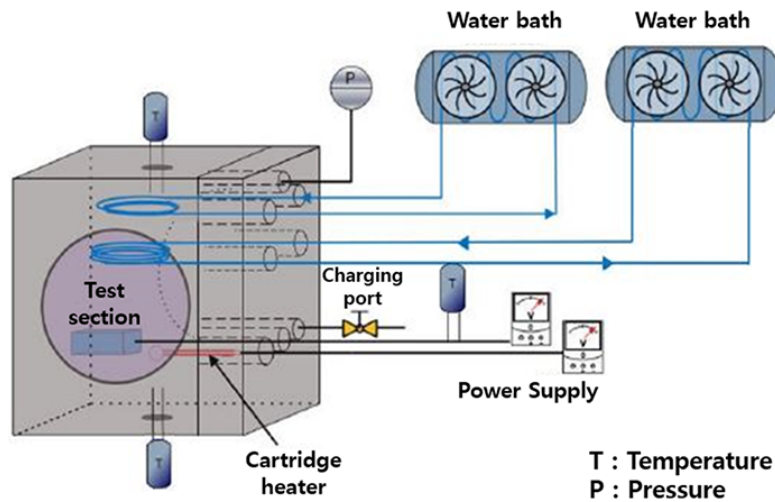
FIG. 3: Schematic drawing of the test apparatus

was chosen because commercial refrigeration chillers operate at the temperature; the 26.7°C was chosen because it is the normal room temperature. The apparatus had a charging line and an evacuating line. The evacuating line was connected to a positive displacement vacuum pump. Before each test, the test sample was thoroughly cleaned with acetone. Then, the test sample was operated at a maximum heat flux (approximately 120 kW/m^2) for an hour to degas the test sample and the pool. This procedure was proposed by Bergles and Chyu (1982). Then, the data were taken decreasing the heat flux. Throughout the test, the liquid level was maintained at 10 cm above the test sample.

The heat transfer coefficient (h) was determined by the heat flux (q) over wall superheat ($T_w - T_{sat}$). The input power to the heater was measured by a precision watt-meter (Chitai 2402A). The thermocouples and the pressure transducer were connected to the data logger (Fluke 2645A). The thermocouples and the transducer were calibrated and checked for repeatability. The accuracy of the temperature measurement was ± 0.15°C and the accuracy of the pressure measurement was ± 0.13% of full scale. The boiling surface temperature was determined by extrapolating the thermocouple temperatures to the tube wall using Fourier's law. An error analysis was conducted following the procedure proposed by Kline and McClintock (1953). The uncertainty in the heat transfer coefficient is estimated to be ± 3.2% at the maximum heat flux (120 kW/m^2) and ± 7.3% at a low heat flux (4 kW/m^2).

4. RESULTS AND DISCUSSIONS

4.1 Smooth Surface

Prior to the tests on enhanced surfaces, studies were conducted on the smooth surface. The boiling heat transfer coefficients of the smooth surface were taken at 4.4°C and 26.7°C (Fig. 4). The heat transfer coefficient increases as the heat flux or the saturation temperature increases. At higher heat flux and saturation temperature, more nucleation sites become active, and the heat transfer coefficient increases. The present data are compared with the Cooper (1982) correlation
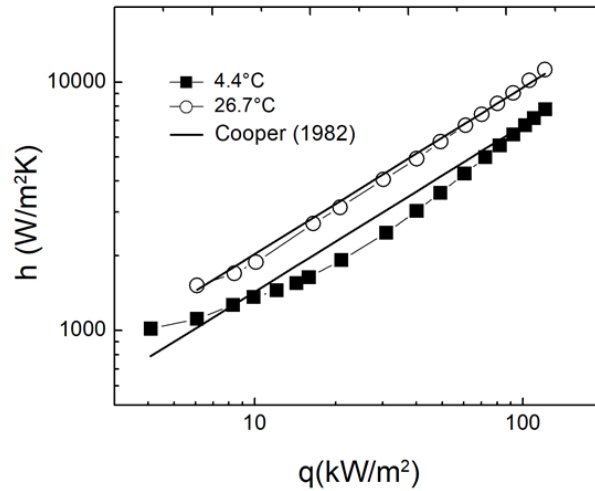
FIG. 4: Smooth surface data compared with Cooper (1982) correlation

in Fig. 4, which shows that all the data are predicted within $\pm$ 20%. The Cooper correlation is known to predict the pool boiling data of refrigerants reasonably well.

4.2 Bubble Behavior

The bubble behavior was photographed using a high speed camera. A sample photo of the bubble is shown in Fig. 5. From the photo, the bubble diameter was calculated using the equation suggested by Lee et al. (2004).

$$d = 2 \left\{ \frac{1}{2} B^2 A + \frac{3}{4} B^2 \left(D - \frac{D^3}{3E^2} \right) \right\}^{1/3} \tag{1}$$

$$E = \sqrt{\frac{D^2}{1 - (C/2)^2/B^2}} \tag{2}$$

Bubble growth data were also obtained from the photos, and typical ones are shown in Fig. 6. The bubble departure diameter and the frequency were determined by averaging those from ten consecutive cycles for each active pore, and then averaging those from three to five active pores.

Bubble departure diameters and frequencies are summarized in Table 1 for the smooth and the nine pore/sub-tunnel samples at the heat flux of 8 kW/m^2. Table 1 shows that the bubble departure diameter of the pored sample is larger than that of the smooth sample. The bubble departure diameter increases as the pore diameter increases, or the saturation temperature decreases. However, it is relatively independent of the pore pitch. Table 1 shows that the bubble frequency data do not show a consistent trend. Generally, the bubble frequency decreases as pore diameter or pore pitch increases with some exceptions. This issue will be elaborated in the later section.
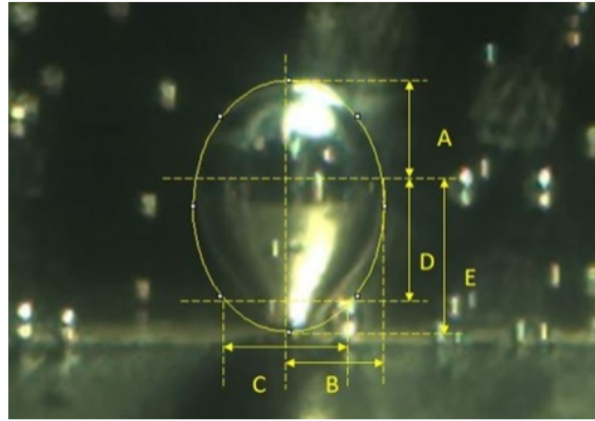
FIG. 5: A photo showing the departing bubble and the dimensions used to determine the bubble departure diameter
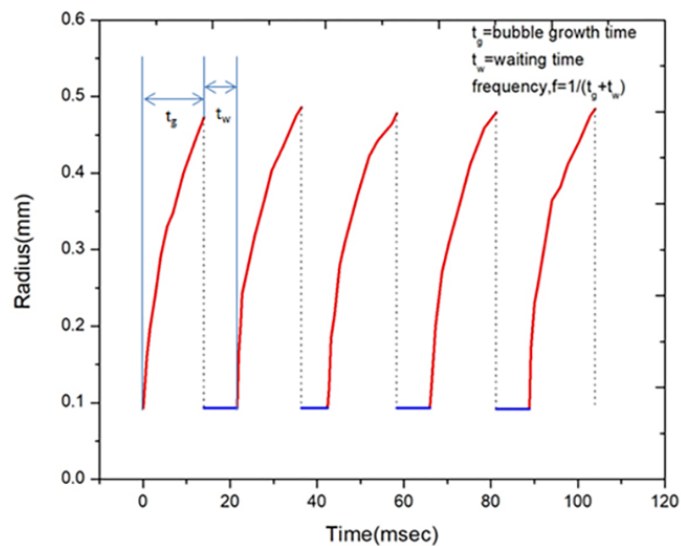

**FIG. 6:** Bubble growth behavior of the sample 0.2/1.5 at 4.4°C and 8 kW/m^2

4.3 Pore/Sub-Tunnel Surfaces

The heat transfer coefficients of the present enhanced tubes are shown in Figs. 7–12. Figures 7, 8, and 9 show the effect of pore diameter for a given pore pitch, and Figs. 10, 11, and 12 show the effect of pore pitch for a given pore diameter. Data are provided for two saturation temperatures (4.4°C and 26.7°C). All figures show that the heat transfer coefficients at 26.7°C are higher than those at 4.4°C.

Figure 7 shows the heat transfer coefficients of the samples having different pore diameters at fixed pore pitch of 0.75 mm. The smooth sample data are also shown. All pored samples have higher heat transfer coefficients than the smooth sample. Furthermore, the enhancement ratio (heat transfer coefficient of the pored sample divided by that of the smooth sample) decreases

TABLE 1: Bubble dynamic data for present pore/sub-tunnel samples

Samples	d_b(mm)		f (Hz)	
	26.7°C	**4.4°C**	**26.7°C**	**4.4°C**
0.1/0.75	0.67	0.76	31.2	34.6
0.1/1.5	0.66	0.75	42.9	45.4
0.1/3.0	0.62	0.73	21.2	24.4
0.2/0.75	0.87	0.97	26.8	32.0
0.2/1.5	0.86	0.94	42.5	48.8
0.2/3.0	0.81	0.91	45.0	50.4
0.3/0.75	1.10	1.19	17.4	18.8
0.3/1.5	1.03	1.14	41.1	48.2
0.3/3.0	0.93	1.06	49.0	58.2
Smooth	0.43	0.46	21.2	28.1

(a)

0.1/0.75   0.2/0.75   0.3/0.75

(b)
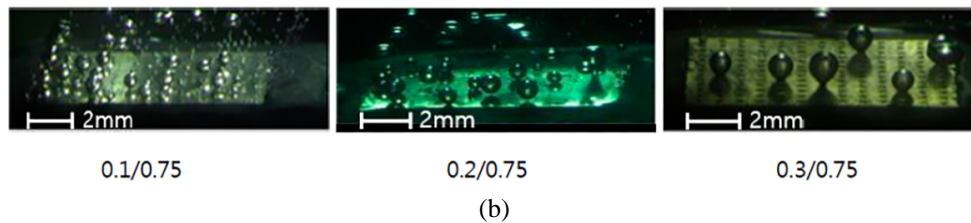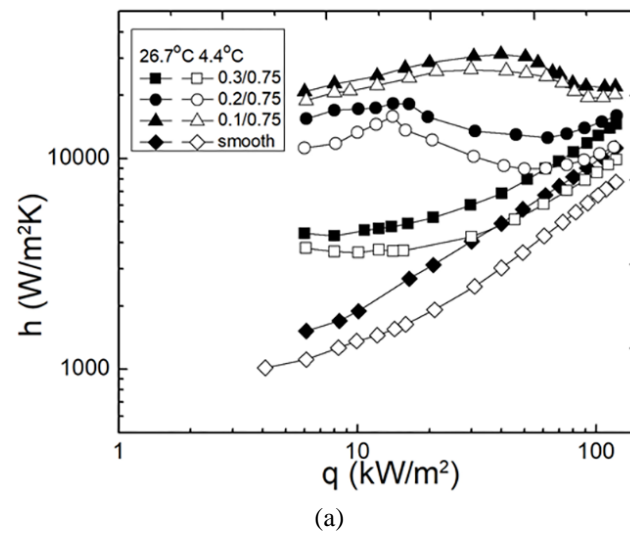
FIG. 7: (a) Heat transfer coefficients and (b) bubble behavior at 8 kW/m^2 and 4.4°C of the pored tubes ($P_p = 0.75$ mm)
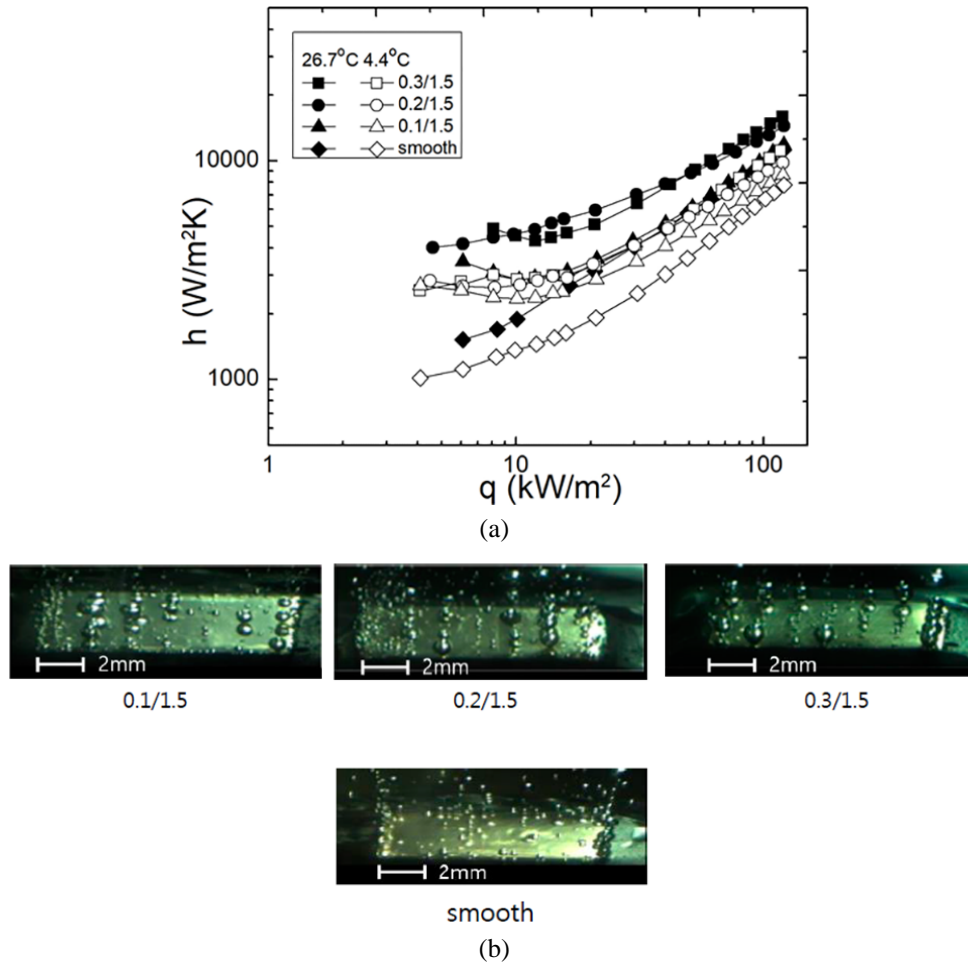
(a)

(b)

FIG. 8: (a) Heat transfer coefficients and (b) bubble behavior at 8 kW/m^2 and 4.4°C of the pored tubes (P_p = 1.5 mm)

as the heat flux increases. Of the three pored samples, 0.3/0.75 yielded the highest heat transfer coefficient, followed by 0.2/0.75 and 0.1/0.75. For the pore/sub-tunnel configuration, the major heat transfer mechanism is thin film evaporation in the sub-tunnel. Furthermore, the evaporation heat flux in the tunnel is obtained from the following equation.

$$q_{tun} = \rho_v i_{lv} N_A \frac{\pi d_b^3}{6} f \tag{3}$$

Table 1 shows that, for the three samples at 26.7°C, the departure diameter increases 64% from 0.67 mm to 1.10 mm as the pore diameter increases from 0.1 mm to 0.3 mm, whereas the frequency decreases 44% from 31.2 Hz to 17.4 Hz. Considering that the evaporation heat flux is proportional to the cube of the departure diameter as shown in Eq. (3), the 64% increase of the bubble diameter for the 0.3/0.75 sample compared with 0.1/0.75 sample appears responsible for the higher heat transfer coefficient of the 0.3/0.75 sample. It is noted that the density of active
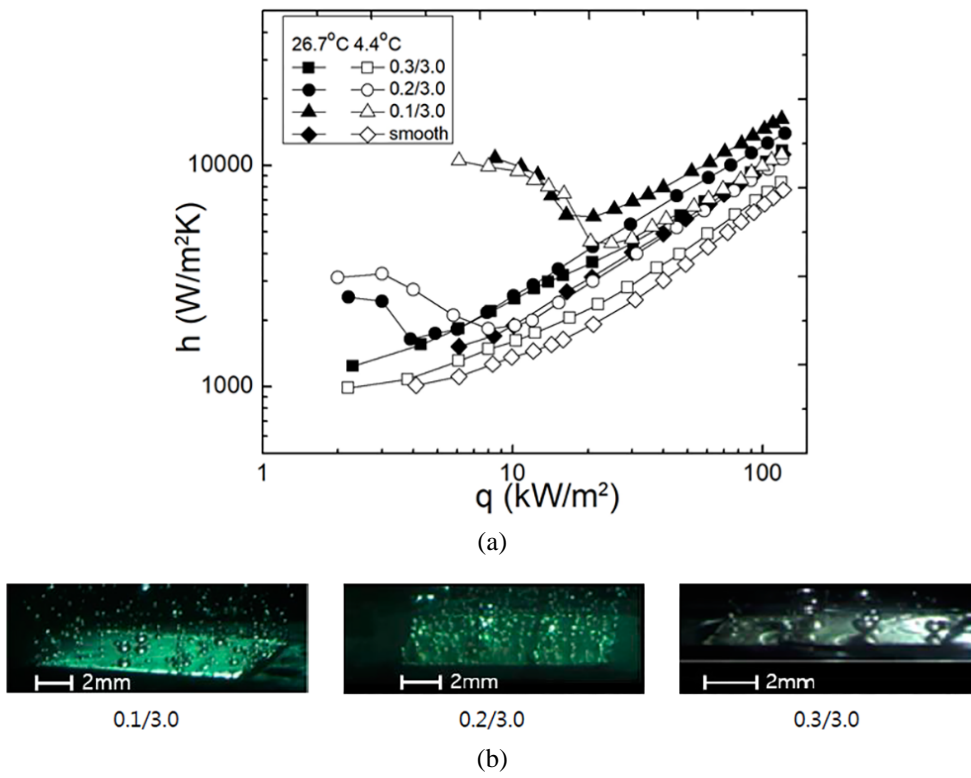
(a)

2mm   2mm   2mm

0.1/3.0   0.2/3.0   0.3/3.0

(b)

FIG. 9: (a) Heat transfer coefficients and (b) bubble behavior at 8 kW/m^2 and 4.4°C of the pored tubes ($P_p = 3.0$ mm)
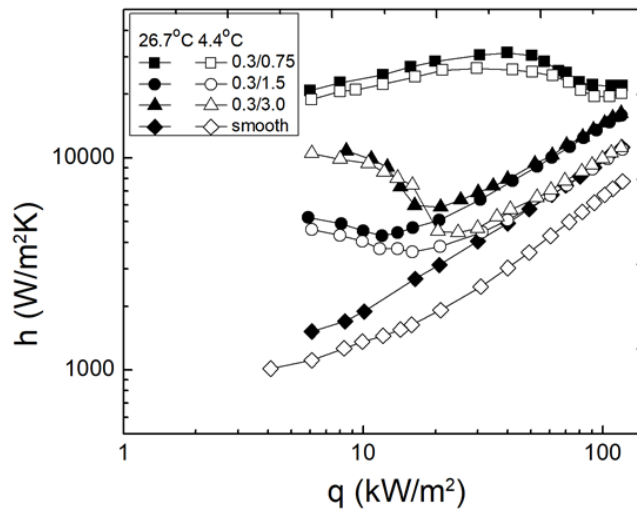

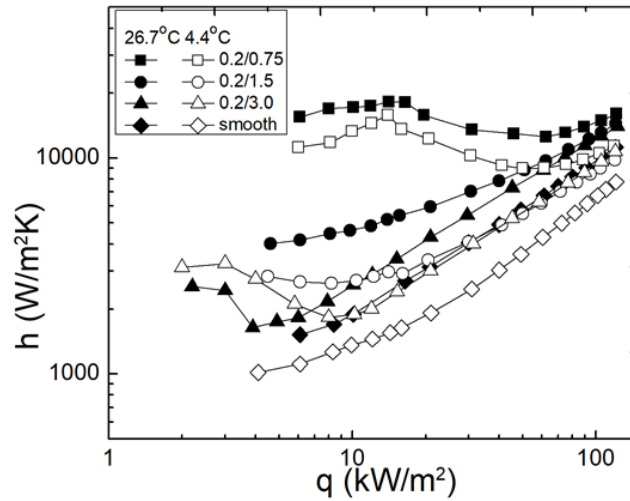**FIG. 10:** Heat transfer coefficients of the pored tubes ($d_p = 0.3$ mm)

FIG. 11: Heat transfer coefficients of the pored tubes ($d_p = 0.2$ mm)
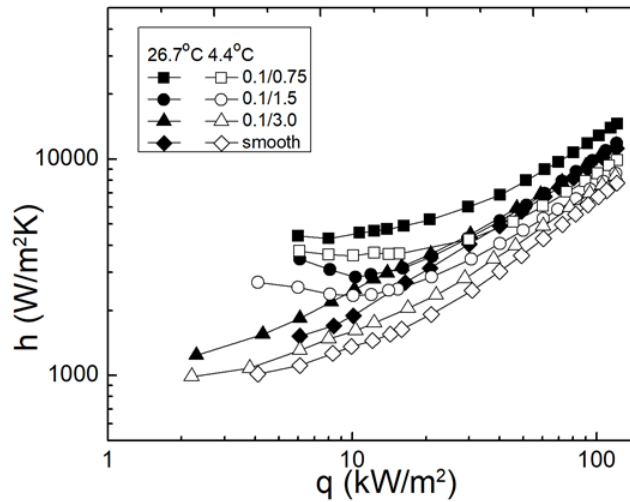

FIG. 12: Heat transfer coefficients and bubble behavior of the pored tubes ($d_p = 0.1$ mm)

nucleation sites (N_A), which also affects the evaporation heat flux, were not measured in the present study due to the limitation of the experimental apparatus. Accompanying photos taken at 8 kW/m^2 and 4.4°C saturation temperature show that, as pore diameter increases, the bubble size gets bigger.

An interesting feature of the boiling curve—increasing, decreasing, and increasing again—occurs in samples 0.2/0.75 and 0.3/0.75. First, the heat transfer coefficient increases due to the increase of more active nucleation sites with the increase of heat flux. Then, with further increase of heat flux, some portion of the tunnels become dry and the heat transfer coefficient decreases. The maximum heat flux was termed as "dry-out heat flux" by Chien and Webb (1998a). At a very high heat flux, all tunnels will dry out, and the heat transfer coefficient will become

approximately similar to that of the smooth sample. This process yields an increasing boiling curve. Although not apparent, the 0.1/0.75 sample also shows a decreasing–increasing boiling curve at a low heat flux.

Figure 8 shows the heat transfer coefficients of samples having pore pitch of 1.5 mm. Similar to the previous case, 0.3/1.5 yielded the highest heat transfer coefficient, followed by 0.2/0.75 and 0.1/0.75. At low heat fluxes, the pored samples yield higher heat transfer coefficients than the smooth sample. As the heat flux increases, however, the heat transfer coefficients tend to merge. Accompanying photos show small bubbles along with large bubbles, which are apparently generated from the plain surface between pores. For comparison purpose, a photo of the smooth sample is included. The bubble size from the smooth sample appears approximately the same as that from the plain surface of the pored samples. Figure 8 also shows decreasing—increasing boiling curves at a low heat flux. The bubble dynamic data in Table 1 shows that, for the three samples at 26.7°C, the departure diameter increases 56% from 0.66 mm to 1.03 mm as the pore diameter increases from 0.1 mm to 0.3 mm, whereas the frequencies are approximately equal. The increased bubble diameter may be responsible for the higher heat transfer coefficient of the 0.3/1.5 sample.

Figure 9 shows the heat transfer coefficients of samples having pore pitch of 3.0 mm. Sample 0.3/3.0 yielded the highest heat transfer coefficient, followed by 0.2/3.0 and 0.1/3.0. At low heat fluxes, the pored samples yield higher heat transfer coefficients than the smooth sample. As the heat flux increases, however, the heat transfer coefficients tend to merge. These samples also show decreasing—increasing boiling curves. Clearly, the "minimum heat flux", where the heat transfer coefficient starts to increase, increases as pore diameter increases, probably due to the delayed tunnel dry-out for the larger pore diameter sample.

Careful inspection of Fig. 7 also shows the same trend of the "minimum heat flux." Accompanying photos show many small bubbles between large bubbles. Note that only 16 pores are available for these 3.0 mm pore pitch samples. The bubble dynamic data in Table 1 shows that, for the three samples at 26.7°C, the departure diameter increases 50% from 0.62 mm to 0.93 mm as the pore diameter increases from 0.1 mm to 0.3 mm. The increased bubble diameter may be responsible for the higher heat transfer coefficient of the 0.3/1.5 sample. It is noted that, for this configuration of large pore pitch of 3.0 mm, the bubble frequency increased as pore diameter increased, contrary to the case of small pore pitch of 0.75 mm. At the medium pore pitch of 1.5 mm, the bubble frequency was approximately the same irrespective of the pore diameter. At the present time, no adequate explanation is possible for this trend. Future investigation on this issue is recommended.

Figure 10 shows the effect of pore pitch on the heat transfer coefficient at fixed pore diameter of 0.3 mm. The highest heat transfer coefficients were obtained for the sample having 0.75 mm pore pitch. Samples having 1.5 mm and 3.0 mm pitch yield approximately the same heat transfer coefficient except at low heat fluxes, where the sample with 3.0 mm pitch yields higher heat transfer coefficient. As pore pitch decreases, the number of pores increases approximately in proportion to the square of pitch ratio. The number of pores was 16, 49, and 169 for 3.0 mm, 1.5 mm, 0.75 mm pitch, respectively. The large number of active pores appears responsible for the high heat transfer coefficients of the sample with 0.75 mm pitch. Figure 10 shows that, at low heat fluxes, the sample with 3.0 mm pitch yields higher heat transfer coefficient than the sample with 1.5 mm pitch. As discussed by Chien and Webb (1998a,b), there exists an optimum pore pitch for a specific heat flux range. If the pore pitch is too small at a low heat flux, the tunnel is likely to be flooded by the liquid, and the heat transfer coefficient is decreased. If the pore pitch is too large at a high heat flux, the tunnel will dry out due to the insufficient liquid supply. It is

likely that, at a low heat flux, the 1.5 mm pitch is so small that the heat transfer coefficients are smaller than those of the 3.0 mm pitch.

Figure 11 shows the heat transfer coefficients of the samples having 0.2 mm pore diameter. A similar trend with the previous 0.3 mm pore diameter case is shown. The highest heat transfer coefficient is obtained for the sample with 0.75 mm pitch, followed by 1.5 mm and 3.0 mm pitch. The 0.1 mm pore diameter data in Fig. 12 show the same trend. The bubble dynamic data in Table 1 shows that the bubble frequency increases as the pore pitch increases except for the case of 0.1 mm pore diameter, where maximum bubble frequency was obtained at the intermediate pore pitch of 1.5 mm. As the pore pitch increases, the density of active pore will decrease, and the bubble frequency per pore will increase. For the case of 1.0 mm pore diameter, no adequate explanation is available at present.

4.4 Comparison with Theoretical Models

The present data are compared with available theoretical models (Nakayama et al., 1980b; Chien and Webb, 1998e; Pastuszko and Wojcik, 2015), and the results are shown in Figs. 13 and 14. Details of the models are summarized in the Appendix. Figure 13 shows the comparison of the data with the predictions by the Nakayama et al. (1980b) model. Significant overprediction (RMSE of 49.0) is noted. As discussed above, the Nakayama model contains six empirical constants, which were determined from the best-fit of their data (Nakayama et al., 1980a). The model may be valid within the tested pore dimensions. The major difference between the present pore dimensions with those of Nakayama et al. (1980a) is tunnel pitch. Compared with the present tunnel pitches (0.75 mm, 1.5 mm, and 3.0 mm), those of Nakayama et al. are very small (from 0.4 mm to 0.6 mm). In addition, the pore pitches of Nakayama et al. (1980a) (from 0.6 mm to 0.72 mm) are also smaller than those of the present study (0.75 mm, 1.5 mm, and 3.0 mm), which implies a greater number of pores per unit area. It appears that overprediction of Nakayama et al. (1980b) of the present data may be related with the pore density difference between two samples.
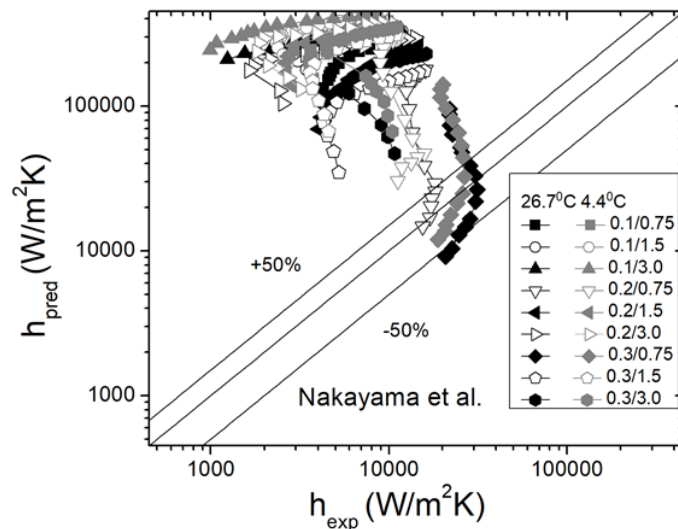

FIG. 13: The present data compared with predictions by Nakayama et al. (1980b)
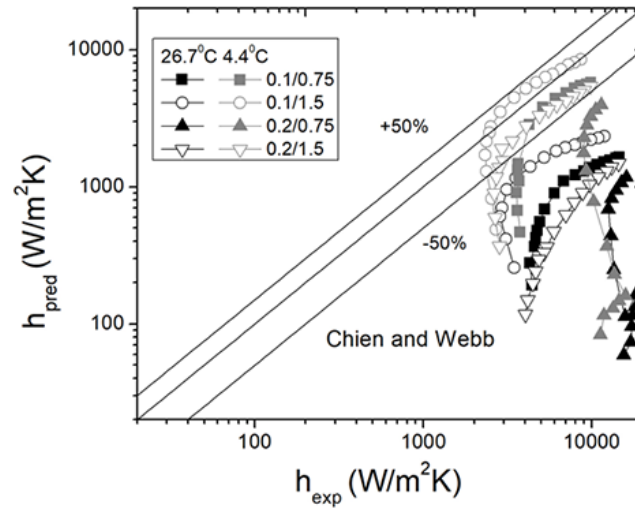
FIG. 14: The present data compared with predictions by Chien and Webb (1998e)

The present data are also compared with the Chien and Webb (1988e) model, and the results are shown in Fig. 14. Note that only limited data, which yielded converged solutions, are presented. Differing from Nakayama et al. (1980b), most of the data are underpredicted (RMSE of 62.2). As discussed, the Chien and Webb model has two empirical constants, which were determined from their own data. In the Chien and Webb model, the total heat transfer is obtained by summing up the latent heat transfer by thin film evaporation within sub-tunnels and the sensible heat transfer by bubble agitation on top of the heating surfaces. Furthermore, the latent heat transfer is assumed to be proportional to the number of liquid menisci formed at the edges of the tunnel. In this case, the number of liquid menisci becomes a determining factor for the latent heat transfer. Differing from the present samples, where tunnels were sharply machined, Chien and Webb samples were made from low fin tubes by wrapping the fin tips with pierced copper foils. Generally, low fin tubes are made by cold rolling the smooth tube, and the resulting fin base has a rounded edge, which may not form a liquid meniscus. If this is true, a model based on rounded-edge low fin tube data may underpredict the data obtained from the surface having machined sub-tunnels.

The present data are compared with the Pastuszko and Wojcik (2015) model (Fig. 15). Compared with previous two models, better results (RMSE of 3.80) were obtained. Careful inspection of the predictions with the data revealed that the prediction was relatively good at high heat fluxes. However, they gradually overpredicted the data as the heat flux decreased. In fact, the Pastuszko and Wojcik model assumes constant nucleation site density, which is sorely dependent on pore dimensions and bubble departure diameter. Their nucleate site density is expressed as the ratio of the maximum possible number of active pores in the tunnel area to total surface area. Refer to Fig. 16 for details.

$$N_A = \frac{4 W_{tun} P_{tun}}{\pi d_b^2} \frac{1}{P_{tun}^2} = \frac{4 W_{tun}}{\pi d_b^2} \frac{1}{P_{tun}} \tag{4}$$

However, there is much experimental evidence that nucleate site density increases as heat flux increases (Nakayama et al., 1980a; Chien and Webb, 1998c,d). Thus, it was decided to
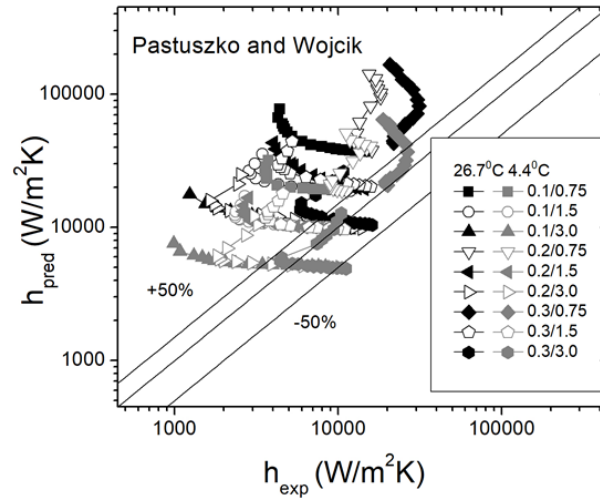
FIG. 15: The present data compared with predictions by Pastuszko and Wojcik (2015)
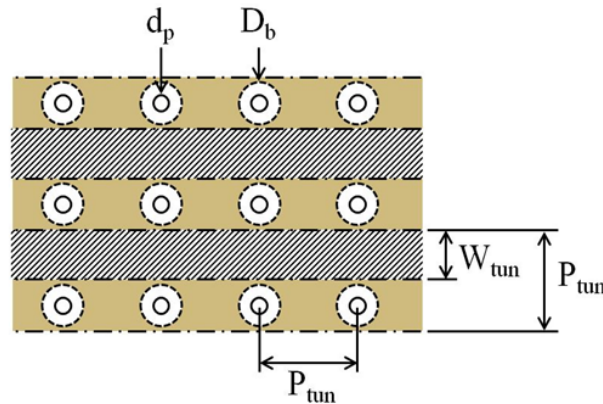

FIG. 16: The present data compared with predictions by the modified Pastuszko and Wojcik model

incorporate the heat flux-dependent nucleation site density function to the Pastuszko and Wojcik model. The present model modifies the nucleate site density equation [Eq. (5)] by incorporating the effect of heat flux.

$$N_A = \frac{4}{\pi d_b^2} \frac{W_{tun}}{P_{tun}} q^{0.062 \ln(q) - 0.82} \tag{5}$$

Predicted nucleation site densities by Eq. (5) are compared with those from photos in Fig. 17 for three samples (0.1/0.75, 0.2/0.75, 0.3/0.75). At 8 kW/m^2, the predicted numbers are 5, 7, and 11 for 0.3/0.75, 0.2/0.75, and 0.1/0.75, respectively, whereas those from photos are approximately 7, 11, and 15. Discrepancies between the predicted values and the measured ones should be accounted for in a future refined model.

Another modification was made on the external heat flux. Exiting models assume that the total heat flux is the addition of the heat flux from the sub-tunnel and that from the external surface. Furthermore, the external heat flux is calculated with consideration of the bubbles generated from

(a)
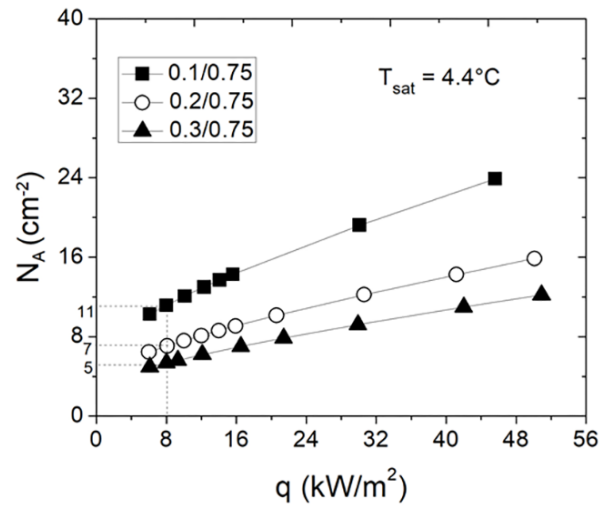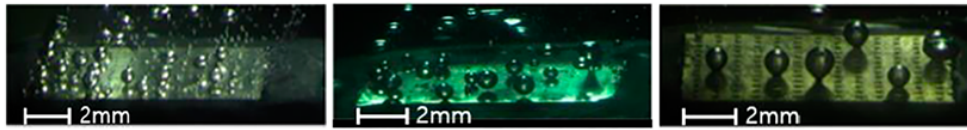
(b)

FIG. 17: Nucleate site density predicted by the present model [Eq. (5)] and corresponding photos (a) Nucleate site density predicted by the present model [Eq. (6)]; (b) Bubble behavior at 8 kW/m^2 and 4.4°C

the pores. This may be true for the case of 0.75 mm pore pitch, where bubble departure diameter is comparable with the pore pitch. For larger pore pitches, however, there exists quite an area which is not influenced by the pore-generated bubbles. Figures 7 and 8 indeed show that small bubbles are generated from the surface between pores. Thus, the present model incorporated the heat transfer from the un-pored plain surface as follows.

$$q = q_{tun} + q_{ex,pore} + q_{ex,plain} \left(\frac{A_{plain}}{A} \right) \qquad (6)$$

The heat flux for the un-pored plain surface was obtained from the Cooper (1982) correlation. Figure 18 shows that the modified model significantly improved the predictability. Approximately 70% of the data are predicted within ± 50%. Throughout the present study, bubble dynamic data including bubble departure diameter and bubble frequency were measured (although nucleation site density data are missing). Refined prediction model may include those bubble dynamic data, which is under progress.

5. CONCLUSIONS

In this study, nine enhanced surfaces having circular pores and rectangular sub-tunnels were made (pore diameter from 0.1 mm to 0.3 mm, pore pitch from 0.75 mm to 3.0 mm), and nucleate
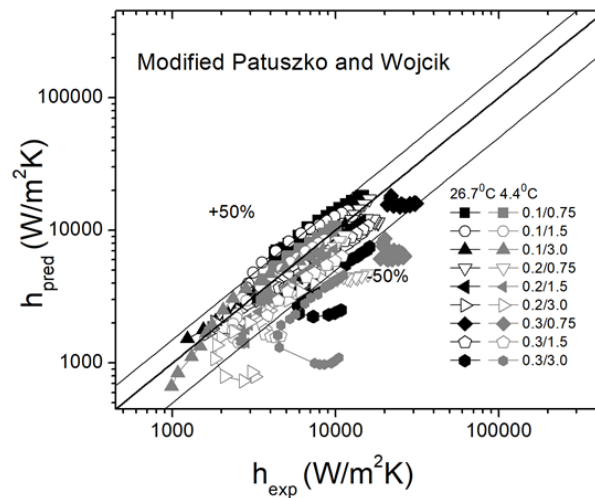
FIG. 18: The present data compared with predictions by the modified Pastuszko and Wojcik model

boiling tests were conducted using R-134a under horizontal position. Listed below are major conclusions.

1. The heat transfer coefficient increased as the pore size increased, at least for the investigated test range. The reason may be attributed to the increased bubble departure diameter with the pore diameter.

2. The heat transfer coefficient increased as the pore pitch decreased. As pore pitch decreased, the number of pores increased approximately in proportion to the square of pitch ratio. Increased active nucleation site density appears responsible for the high heat transfer coefficients.

3. Existing theoretical models do not adequately predict the present data. A new model was proposed by modifying the nucleation site density model of Pastuszko and Wojcik (2015), which predicted 70% of the present data within $\pm$ 50%.

ACKNOWLEDGMENT

REFERENCES

Balaji, D., Velraj, R., and Ramana Murthy, M.V., A Review of the Role of Passive Techniques on Heat Transfer Enhancement of Horizontal Tube Falling Film and Flooded Evaporators, *J. Enhanced Heat Transf.*, vol. **25**, pp. 239–282, 2018.

Bergles, A.E. and Chyu, M.C., Characteristics of Nucleate Pool Boiling from Porous Metallic Coatings, *J. Heat Transf.,* vol. **104**, pp. 279–285, 1982.

Chen, Y., Groll, M., Mertz, R., and Kulenovic, R., Pool Boiling Heat Transfer of Propane, Isobutane and Their Mixtures on Enhanced Tubes with Reentrant Channels, *Int. J. Heat Mass Transf.*, vol. **48**, pp. 2310–2322, 2005.

Chien, L.-H. and Chang, C.-C., Enhancement of Pool Boiling on Structured Surfaces using HFC-4310 and Water, *J. Enhanced Heat Transf.*, vol. **11**, pp. 23–44, 2004.

Chien, L.-H. and Webb, R.L., A Parametric Study of Nucleate Boiling on Structured Surfaces, Part I: Effect of Tunnel Dimensions, *J. Heat Transf.*, vol. **120**, pp. 1042–1048, 1998a.

Chien, L.-H. and Webb, R.L., A Parametric Study of Nucleate Boiling on Structured Surfaces, Part II: Effect of Pore Diameter and Pore Pitch, *J. Heat Transf.*, vol. **120**, pp. 1049–1054, 1998b.

Chien, L.-H. and Webb, R.L., Measurement of Bubble Dynamics on an Enhanced Boiling Surface, *Exp. Thermal Fluid Sci.*, vol. **16**, pp. 177–186, 1998c.

Chien, L.-H. and Webb, R.L., Visualization of Pool Boiling on Enhanced Surfaces, *Exp. Thermal Fluid Sci.*, vol. **16**, pp. 332–341, 1998d.

Chien, L.-H. and Webb, R.L., A Nucleate Boiling Model for Structured Enhanced Surfaces, *Int. J. Heat Mass Transf.*, vol. **41**, pp. 2183–2195, 1998e.

Cooper, M.G., Correlations for Nucleate Boiling: Formulation using Reduced Properties, *Phys.-Chem. Hydrodynam.*, vol. **3**, no. 2, pp. 89–111, 1982.

Gorgy, E. and Eckels, S., Local Heat Transfer Coefficient for Pool Boiling of R-134a and R-123 on Smooth and Enhanced Tubes, *Int. J. Heat Mass Transf.*, vol. **55**, pp. 3021–3028, 2012.

Kim, N.-H. and Choi, K.-K., Nucleate Pool Boiling on Structured Enhanced Tubes Having Pores with Connecting Gaps, *Int. J. Heat Mass Transf.*, vol. **44**, pp. 17–28, 2001.

Kline, S.J. and McClintock, F.A., The Description of Uncertainties in Single Sample Experiments, *Mechan. Eng.*, vol. **75**, pp. 3–9, 1953.

Lee, H.C., Kim, S., Oh, B.D., and Kim, M.H., Single Bubble Growth in Saturated Pool Boiling of Binary Mixtures, *Int. J. Multiphase Flow*, vol. **20**, pp. 697–710, 2004.

Mikic, B.B. and Rohsenow, W.M., A New Correlation for Pool Boiling Data Including the Effect of Heating Surface Characteristics, *J. Heat Transf.*, vol. **91**, pp. 245–250, 1969.

Nakayama, W., Daikoku, T., Kuwahara, H., and Nakajima, T., Dynamic Model of Enhanced Boiling Heat Transfer on Porous Surfaces, Part I: Experimental Investigation, *J. Heat Transf.*, vol. **102**, pp. 445–450, 1980a.

Nakayama, W., Daikoku, T., Kuwahara, H., and Nakajima, T., Dynamic Model of Enhanced Boiling Heat Transfer on Porous Surfaces, Part II: Analytical Modeling, *J. Heat Transf.*, vol. **102**, pp. 451–456, 1980b.

Orman, L., Enhancement of Pool Boiling Heat Transfer with Pin-Fin Microstructures, *J. Enhanced Heat Transf.*, vol. **23**, pp. 137–153, 2016.

Pastuszko, R. and Wojcik, T.M., Experimental Investigations and a Simplified Model for Pool Boiling on Microfins with Sintered Perforated Foil, *Exp. Thermal Fluid Sci.*, vol. **63**, pp. 34–44, 2015.

Ramaswamy, C., Joshi, Y., Nakayama, W., and Johnson, W.B., Semi-Analytic Model for Boiling from Enhanced Surfaces, *Int. J. Heat Mass Transf.*, vol. **46**, pp. 4257–4269, 2003.

Ribatski, G. and Thome, J.R., Nucleate Boiling Heat Transfer of R-134a on Enhanced Tubes, *Appl. Thermal Eng.*, vol. **26**, pp. 1018–1031, 2006.

Rooyen, E. and Thome, J.R., Pool Boiling Data and Prediction Method of Enhanced Boiling Tubes with R-134a, R-236fa and R-1234ze(E), *Int. J. Refrigeration*, vol. **36**, pp. 447–455, 2013.

Webb, R.L. and Pais, C., Nucleate Pool Boiling Data for Five Refrigerants on Plain, Integral-Fin and Enhanced Tube Geometries, *Int. J. Heat Mass Transf.*, vol. **35**, no. 8, pp. 1893–1904, 1992.

Yang, C.-Y. and Fan, C.-F., Pool Boiling of Refrigerant R-134a and R-404A on Porous and Structured Tubes, Part II. Heat Transfer Performance, *J. Enhanced Heat Transf.*, vol. **13**, pp. 85–97, 2006.

APPENDIX

1. Nakayama et al. (1980b) Model

In the Nakayama et al. model, the total heat flux is obtained from

$$q = q_{tun} + q_{ex} \tag{A.1}$$

The evaporation heat flux in the tunnels (q_{tun}) is expressed by

$$q_{tun} = (m_{lg} + m_{lw})i_{lv}/[(t_g + t_w)A] \tag{A.2}$$

where m_{lg} is the evaporated liquid mass during waiting period, m_{lw} is the evaporated liquid mass during growth period, and A is the base heat transfer area. The waiting period t_w, the growth period t_g, m_{l1}, m_{l2} are obtained from the following equations:

$$t_w = \frac{V_{vm}i_{iv}}{k_l C_{t1}} \left\{ \frac{\rho_{vmw}(i_{lv} - RT_{vo})}{RT_{vo}^2} \ln\left(\frac{T_v - T_{vo}}{T_w - T_{vw}} \right) + \frac{\rho_{vmw}}{\Delta T_{tw}} \ln\left(\frac{V_{vw}}{V_{tun}} \right) \right\} \tag{A.3}$$

$$t_g = \theta_2 \sqrt{\frac{\rho_l d_p^3}{8\sigma}} \tag{A.4}$$

$$\theta_2 = \sqrt{\frac{\eta_d^3}{5.242} \left\{ 0.1457 - 0.0329 C_0 \left(\frac{\rho_{vmg}}{\rho_l} \right) \eta_d^4 \right\}} \tag{A.5}$$

$$\eta_d = \frac{d_b}{d_p} \left\{ 1 + \sqrt{1 - (d_p/d_b)^2} \right\} \tag{A.6}$$

$$d_b = C_b \sqrt{\frac{2\sigma}{g(\rho_l - \rho_{vmg})}} \tag{A.7}$$

$$m_{lw} = V_{vm}(\rho_{vw} - \rho_{v0}) + N(\pi d_o^3/12)\rho_{vmw} \tag{A.8}$$

$$m_{lg} = C_{t2}t_g k_l \Delta T_{tg}/i_{lv} \tag{A.9}$$

Here, subscript '0' denotes initial value, 'm' denotes mean value, 'w' denotes waiting period, and 'g' denotes growth period. The external heat flux (q_{ex}) is obtained from the following equations.

$$q_{ex} = \left(\frac{\Delta T}{C_q} \right)^{5/3} \left(N_A^{1/3} \right) \tag{A.10}$$

$$\frac{N_A}{NA} = \frac{\Phi\theta_2 - \xi(\xi^2 + 3) + 4}{\eta_d(\eta_d^2 + 3) - 4} \tag{A.11}$$

$$\Phi = \frac{24 k_l C_{t2} \Delta T_{tg}}{\rho_{vm} i_{lv} \sqrt{2\sigma/d_p \rho_l} N \pi d_p^2} \tag{A.12}$$

$$\xi = -C_3 \left\{ \frac{8(m_{lg} + m_{lw})}{\rho_l N \pi d_p^3} \right\}^{1/3} \tag{A.13}$$

The empirical constants are as follows.

$$C_0 = 0, \quad C_b = 0.442, \quad C_3 = 3.172, \quad C_{t1} = 313, \quad C_{t2} = 27700, \quad C_q = 1.95$$

2. Chien and Webb (1998e) Model

In the Chien and Webb model, the total heat flux is obtained from

$$q = q_{tun} + q_{ex} \tag{A.14}$$

The evaporation heat flux in the tunnels (q_{tun}) is obtained by iteratively solving the following equations:

$$\int_0^{t_w} \frac{dq_{tun}/dt}{\Delta T} dt = \frac{V_{vm}i_{lv}}{A_{tun}} \left\{ \frac{\rho_v(i_{iv} - RT_{v0})}{RT_{v0}^2} \ln\left(\frac{T_w - T_{v0}}{T_w - T_{vw}}\right) + \frac{\rho_v}{\Delta T_{tw}} \ln\left(\frac{V_{vw}}{V_{tun}}\right) \right\} \tag{A.15}$$

$$q_{tun} = \int_0^{1/f} \frac{\Delta T}{A_{tun}} \left[2LN_m \int_0^{\pi/4} \frac{k_l R_m(t)}{\{R_m(t) + \delta_{ne}(t)s(\phi) - R_m(t)\}} d\phi \right] dt \tag{A.16}$$

$$d_b = d_p \left\{ \frac{\text{Bo} + \sqrt{\text{Bo}^2 + 2304(96/\text{Bo} - 3)}}{192 - 6\text{Bo}} \right\}^{1/2} \tag{A.17}$$

$$t_g = 0.0296 \left\{ \frac{7}{\pi} \frac{\rho_l T_{sat}}{i_{lv}\rho_v \Delta T} \frac{(d_b + d_p)}{(d_b - d_p)} \right\}^{1/2} \left(\frac{d_b - d_p}{2}\right) \tag{A.18}$$

$$f = \frac{1}{t_w + t_g} \tag{A.19}$$

The external heat flux (q_{ex}) is obtained from the following equations:

$$q_{ex} = 2\sqrt{\pi k_l \rho_l c_p f} d_b^2 N_A \Delta T \left\{ 1 + \left(\frac{4.24\pi}{\text{Pr}^{1/6}}\right)^2 \right\}^{1/2} \tag{A.20}$$

$$N_A = \frac{q_{tun}}{\rho_v i_{iv} f(\pi d_b^3)/6} \tag{A.21}$$

3. Pastuszko and Wojcik (2015) Model

In the Pastuszko and Wojcik model, the total heat flux is obtained from

$$q = q_{tun} + q_{ex} \tag{A.22}$$

The evaporation heat flux in the tunnels (q_{tun}) is expressed by

$$q_{tun} = \rho_v i_{lv} N_A \frac{\pi d_b^3}{6} f \tag{A.23}$$

where N_A is the mean density of nucleation sites, which is expressed as follows:

$$N_A = \frac{4W_{tun}}{\pi d_b^2} \frac{1}{P_{tun}} \tag{A.24}$$

Here, $4W_{tun}/\pi d_b^2$ denotes number of active pores per tunnel, which is obtained by dividing the tunnel width by the cross-sectional area of the departing bubble. The bubble departure diameter (d_b) and bubble generation frequency (f) are obtained from

$$d_b = \left[\frac{6\sigma d_p}{g(\rho_l - \rho_v)} \right] \tag{A.25}$$

$$f = \frac{1}{t_w + t_g} \tag{A.26}$$

$$t_w = 3\Delta t_g \tag{A.27}$$

$$t_g = \frac{1}{0.0296} \left[\frac{7}{\pi} \frac{\rho_l T_{sat}}{i_{lv} \rho_v \Delta T} \frac{(d_b + d_p)}{(d_b - d_p)} \right]^{1/2} \left(\frac{d_b - d_p}{2} \right) \tag{A.28}$$

The external heat flux (q_{ex}) was obtained from the Mikic and Rohsenow (1969) correlation.

$$q_{ex} = 2\sqrt{\pi k_l \rho_l c_{pl} f} d_b^2 N_A \Delta T_{tip} \tag{A.29}$$